Trivalent actinides and lanthanides incorporation in UMo glass-ceramics

Magaly Tribet, Christophe Jegou, Sylvain Peuget, S Miro, J Delrieu, F. Doreau

To cite this version:

Magaly Tribet, Christophe Jegou, Sylvain Peuget, S Miro, J Delrieu, et al.. Trivalent actinides and lanthanides incorporation in UMo glass-ceramics. Journal of Nuclear Materials, 2023, 585, https://doi.org/10.1016/j.jnucmat.2023.154634. 10.1016/j.jnucmat.2023.154634 . cea-04175125

HAL Id: cea-04175125

https://cea.hal.science/cea-04175125v1

Submitted on 1 Aug 2023

Trivalent actinides and lanthanides incorporation and partitioning in UMo glass-ceramics

M. Tribet[1*], C. Jégou[1], S. Miro[1], J. Delrieu[1], F. Doreau[2], S. Peuget[1]

[1]CEA, DES, ISEC, DPME, Univ Montpellier, Marcoule, France

[2]CEA, DES, ISEC, DMRC, Univ Montpellier, Marcoule, France

*corresponding author, magaly.tribet@cea.fr

1 Abstract

This article focuses on the Am incorporation and location in the UMo-glass ceramic designed to manage fission product solutions enriched in ^{241}Am generated by the reprocessing of UMo spent fuel. This type of glass ceramic contains crystalline phases, which are phosphates, molybdates and zircons, embedded in a durable borosilicate glass matrix.

Two types of UMo-glass ceramics were considered in this study. One type of samples was doped with different amounts of Am and/or Nd to assess the comparative role of Nd versus Am in terms of incorporation, location and microstructure. A second type of sample was doped with ^{244}Cm, in order to specify the behavior of ^{244}Cm compared with that of Nd and Am, with a view to using this short-lived isotope for ageing experiments.

These matrices were characterized by gamma spectrometry and isothermal calorimetry to check the overall homogeneity of Am and Cm, then by Raman spectroscopy, SEM, EPMA and XRD to determine the microstructure and the actinide/Nd distribution in the different phases. The microstructure of the samples was heterogeneous as expected, with the presence of phosphate, molybdate and zircon crystalline phases. A great enrichment of Am, Cm and Nd was observed in the phosphate and molybdate phases compared to the embedding glassy matrix and the zircon crystals. A partition coefficient of around x 6 – 7 for Am and Nd was calculated in these two crystalline phases compared to the mean target doping value. Finally, Nd behaved like trivalent actinides in the UMo matrix and could therefore be considered as a relevant surrogate.

2 Highlights

- UMo waste generated by the reprocessing of UMo spent-fuels from gas-graphite reactors
- UMo glass-ceramic containing phosphate, molybdate and zircon crystalline phases
- In UMo glass-ceramics, crystalline phases are embedded in a glassy matrix
- Am contained in the UMo waste
- Am, Cm and Nd partitioning measured in the UMo glass-ceramic conditioning material
- Nd, an Am/Cm good surrogate with respect to its partitioning into the various phases
- Microstructure of actinide(III) doped UMo-glass ceramics

3 Introduction

Vitrification process has been currently used for decades in many countries to immobilize high-level nuclear waste [1]. The first difficulty in designing a waste package is to find the glass formulation able to chemically incorporate or solubilize the chemical elements contained in the waste. The glass formulations must be compatible with an elaboration by vitrification processes suitable for industrial production in a radioactive environment, and must also produce a material that meets long-term behavior requirements [2, 3]. In some cases, the waste to immobilize could be too complex in terms of chemical composition, or loading rate. In these cases, the waste is not fitted anymore to be easily incorporated in a durable borosilicate homogeneous glass. In such cases, glass-ceramic matrices (GCM) could be an alternative way to confine high amounts of high-level waste [4-8] and could offer a flexibility in the management of waste streams to be vitrified [9, 10].

In the specific case of the fission products solutions generated by the reprocessing of UMo spent-fuels, which were used in the past in gas-graphite reactors, molybdenum and phosphorus are the major chemical elements of the waste. However, among the chemical elements of the reprocessing waste, molybdenum is one of the most difficult to incorporate in the borosilicate glasses commonly used [2, 11, 12]. In order to meet the expectations in terms of Mo and P incorporation [13-15], it has thus been necessary to develop a specific glass formulation for this wasteform [13, 14, 16], called UMo glass-ceramic. In this UMo matrix, the formation of crystallized phases during the cooling after melting was observed and led to the formation of phosphate, molybdate and zircon phases, embedded in a durable glassy borosilicate matrix [14, 17].

It should also be noted that UMo waste solutions were enriched with americium (Am) and that UMo matrices are intended for geological disposal. The behavior of this UMo matrix over geological timescale (thousands of years) has thus to be predicted as best as possible: the question of the Am location in the glass-ceramic is of first importance to asses its long-term behavior because of the quite short half-life of the ^{241}Am isotope ($T_{1/2}$ = 432 years) regarding to the geological timescale and the subsequent potential alpha decay damage induced in the matrix with time. Such studies, performed on radioactive materials, requires an implementation in hot cell facilities. Such an approach is very expensive and needs at least several years to be implemented. Moreover, only few experimental techniques are available to characterize these radioactive samples. Consequently, it is of first importance to find a good surrogate of americium in such a matrix in order to complete the knowledge about the quality of the resulting matrix versus elaboration conditions, in terms of radionuclides location. Neodymium is a trivalent lanthanide well known to be a good surrogate of trivalent actinides (Am, Cm) in various matrices: glasses, apatite glass ceramics, ceramics [3, 4, 8, 18-22]. Indeed, Nd and (Am, Cm) are very similar concerning their electronic structure with Nd 4f and (Am, Cm) 5f orbitals very localized and their ionic radius. A first study about Nd-doped UMo-glass ceramics shown that Nd preferentially integrated into phosphate and molybdate crystallized phases [14].

The present study focuses thus on the trivalent actinides (Am and Cm) distribution in the UMo-glass ceramic in order to check the hypothesis of its possible preferential location and incorporation, based on the Nd non-radioactive simulant. Such an information would help better understanding the Am location in the industrial UMo waste matrix and assessing the use of the ^{244}Cm (as a surrogate of Am) for ageing studies carried out over periods of a few years. Indeed, thanks to its short half-life (T1/2 ~ 18 years), the ^{244}Cm is currently used to mimic the level of alpha decay dose - and the subsequent damage - that the different phases could receive with time, and thus, makes possible to predict the behavior of the real material containing Am over geological periods of time. This methodology is commonly performed on HLW glasses [2, 20] or ceramics [23, 24]. The samples were elaborated in hot cell because of their high radioactivity level. They were then characterized by gamma spectrometry and isothermal calorimetry in order to check for Am and Cm homogeneity and mean amount in the material, by Raman spectroscopy and XRD to identify the crystallized phases and then by SEM and EPMA in order to determine the actinide/Nd distribution between the crystallized phases (molybdate, phosphate and zircon) and the embedding borosilicate glassy phase.

4 Materials and methods

4.1 Glass-ceramics fabrication

Four UMo glass-ceramics were fabricated in the DHA-Atalante hot cells facility at CEA-ISEC (Marcoule research center). Three of them are radioactive materials, respectively doped in term of (LnIII + AnIII in mol%) with 100 % of Am, 75 % of Cm/25 % of Nd and 50 % of Am/50 % of Nd. The last one is a non-radioactive material doped with Nd, but elaborated in the hot cell, under the same conditions than the radioactive samples. The amount of Nd, Am and Cm in the material was chosen to be high enough to be characterized by calorimetry and EPMA. Furthermore, the ^{244}Cm amount and the ^{244}Cm/Nd ratio were calculated to meet the expectations in terms of cristalline phases ageing for a couple of years.

The UMo materials were prepared by melting appropriate amounts of oxides, carbonates and nitrates in Pt/Au-crucibles (15 mm diameter). The curium, the americium and the neodymium elements were added as their oxide form (CmO_2, AmO_2 and Nd_2O_3 respectively). The AmO_2 powder used had an isotopic composition of (99.99 ± 0.02) % ^{241}Am. The amount of CmO_2 powder incorporated in the Cm-doped UMo matrix was determined by isothermal calorimetry: the Cm-doped material contained 0.65wt% of ^{244}Cm which corresponded to 0.86wt% of total curium because of the isotopy of the curium oxide. This sample contains both Cm and Nd, but it is called Cm-doped UMo glass-ceramic hereafter for simplicity. The expected chemical compositions of these materials are presented in Table 1.

elem. molar%	Si	B	Na	Al	Ca	Mo	P	Zr	Zn	Nd	Am	Cm	Others	O
Cm-UMo	13.71	8.52	6.38	2.96	2.32	1.48	0.93	0.57	1.58	0.025	0	0.075	0.82	60.71
Am-UMo	13.13	8.16	6.14	2.66	2.21	1.82	1.14	1.27	1.52	0	0.152	0	0.61	61.17
Am/Nd-UMo	13.13	8.16	6.14	2.66	2.21	1.82	1.14	1.27	1.52	0.076	0.076	0	0.61	61.17
Nd-UMo	13.13	8.16	6.14	2.66	2.21	1.82	1.14	1.27	1.52	0.152	0	0	0.61	61.17

elem. weight%	Si	B	Na	Al	Ca	Mo	P	Zr	Zn	Nd	Am	Cm	Others	O
Cm-UMo	17.91	4.28	6.82	3.71	4.32	6.60	1.34	2.42	4.80	0.17	0.00	0.86	1.59	45.17
Am-UMo	16.58	3.96	6.35	3.23	3.98	7.85	1.59	5.21	4.47	0,00	1.65	0.00	1.15	44.00
Am/Nd-UMo	16.63	3.97	6.37	3.24	3.99	7.88	1.59	5.23	4.48	0.49	0.83	0.00	1.15	44.14
Nd-UMo	16.69	3.99	6.39	3.25	4.01	7.90	1.60	5.24	4.50	0.99	0.00	0.00	1.15	44.29

Table 1: Cm, Am, Am/Nd and Nd-doped UMo glass-ceramic compositions expressed in mol% and in elemental mass% of each element. The global amount of minor elements (Li, Ba, Cr, Mg, Sr, Ni, Fe, Sn, Mn, Cs, Te, Ru, Rh, Y, La, Ce, Pr and U) is referenced as “others”.

Several milliliters of deionized water were added, and the resulting slurry was homogenized by means of an ultrasonic probe for several minutes. After homogenization, the Pt/Au-crucible was placed in an alumina container, loaded in a graphite resistor furnace. The furnace atmosphere was then flushed with Ar for 16h. Melting took place at 1250 °C for 3 hours, under Ar atmosphere. The cooling scenario, described in Figure 1, was different between the Am, the Am/Nd and the Nd-doped materials compared to the Cm-doped material, as for this last material preparation, the thermal scenario was adapted to be as close as possible to that expected at an industrial scale. Pictures of the samples as fabricated and once removed from the crucible are presented in Figure 2.

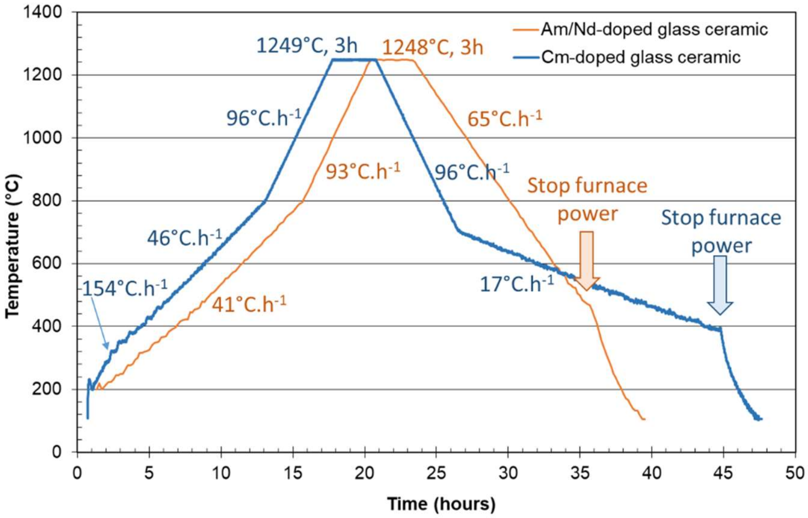

Figure 1: Thermal history of the Am/Nd and Cm-doped UMo glass-ceramic fabrications.

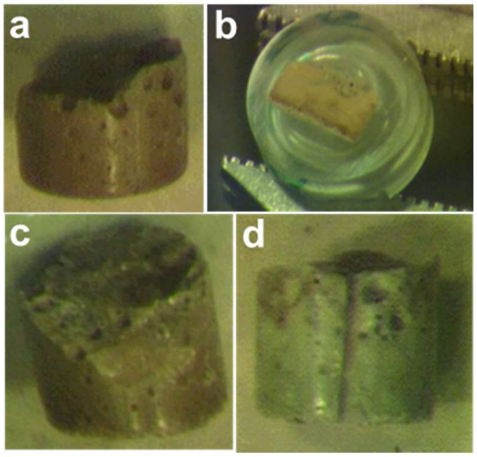

Figure 2: Pictures of the Am (a,b), Am/Nd (c) and the Nd-doped (d) UMo glass-ceramics once the crucible removed. The picture (b) corresponds to the Am-doped UMo glass-ceramic embedded and polished sample.

The glass-ceramics were then cut and prepared for further solid characterizations. A part (or 2 parts as for the Cm-doped sample) of the samples were embedded in epoxy resin and then polished to a micron finish for subsequent structural and microstructural investigations (see Figure 2-b and Figure 3). The remaining part was used for calorimetry measurements (see Figure 3 as an example).

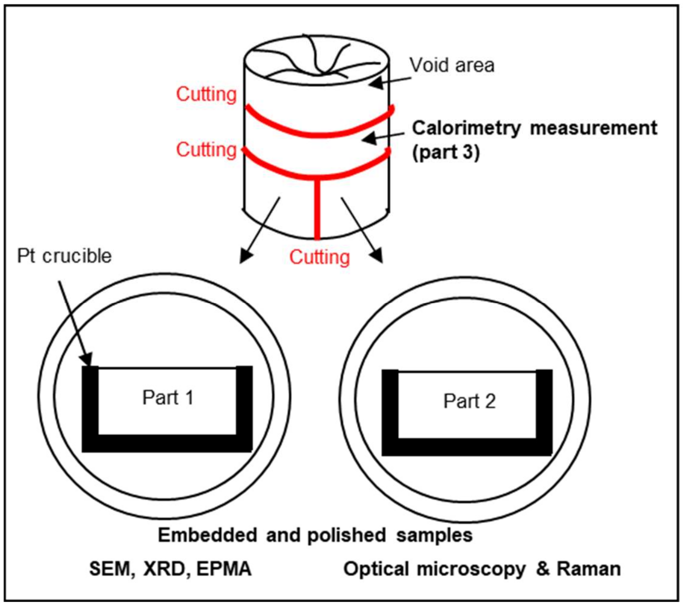

Figure 3: Schematic description of the specimen preparation and use concerning the Cm-doped UMo glass-ceramic.

4.2 Characterization methods

As the materials with Am or Cm are highly radioactive, all the characterizations were performed in hot cells, using shielded characterizations devices.

4.2.1 Actinide content and homogeneity

In order to estimate the homogeneity of the axial Am and Cm distributions, the glass-ceramic rods were analyzed lengthwise by **gamma spectrometry** with a N_2 cooled GeHP EGC15 detector (Camberra, France), on the ^{241}Am line (59.5 keV) and ^{243}Cm lines (228.18 and 277.6 keV). It was performed on the samples as fabricated (Figure 2).

The ^{241}Am and the ^{244}Cm overall contents in the glass-ceramics were determined on samples of around 1 - 2 g weight each, by **isothermal calorimetry.** The heat power generated by the glass-ceramic samples was measured in a SETARAM C80D calorimeter (SETARAM France), with a resolution of 1.2×10^{-7} W and a detection limit of 2×10^{-6} W. The average of 2 heat power measurements was converted into Am and Cm concentrations by considering a decay heat of 0.11 $W.g^{-1}$ for ^{241}Am and 2.83 $W.g^{-1}$ for ^{244}Cm and knowing the isotopic composition of the Am and Cm batches used.

4.2.2 Chemical composition (EPMA) of the different phases

The chemical composition of the actinide-doped glass-ceramics was determined by means of a CAMECA SX 50 electron probe micro analyzer (EPMA, Cameca, France) equipped with four X-ray spectrometers and operated under an acceleration voltage of 20 kV and 30 nA stabilized beam.

Analytical conditions for secondary phases (crystal, standards, K-L-M lines for each element) are detailed in the Table S1 in Supplementary Data. The standard materials used for Am and Cm quantifications were homogeneous ^{241}Am and ^{244}Cm-doped borosilicate glasses fabricated at CEA [25, 26], containing respectively 0.85 wt% of AmO_2 and 1.56 wt% of CmO_2. Their Am and Cm contents were previously very well characterized by mixing various characterization methods: isothermal calorimetry, EPMA, and hot acid dissolution of specimens coupled with ICP-AES analyses.

The relative uncertainty for Am, Cm and Nd content is of 10%, except in the embedded glass phase, where it is specified. The detection limit (LOD) is of 0.01 at%.

From the elemental quantitative measurements, a partition coefficient $(PC)_i$ was calculated for i = Nd, Am and Cm by applying the following equation:

$$PC_i = \frac{(x_i)_{crystalline\ phase}}{(x_i)_{mean\ target\ doping\ value}} \qquad \textit{Equation 1}$$

Were $(x_i)_{\text{crystalline phase}}$ is the atomic value (i.e. quantity in at.%) of Nd, Am or Cm in a given crystalline phase, obtained by EPMA measurements, and $(x_i)_{\text{mean target doping value}}$ is the mean target doping value of Nd, Am or Cm, as expressed in Table 1 in elem mol % (i.e. at. %).

4.2.3 Microstructural and structural characterizations

X-ray diffraction patterns were recorded on the Cm-doped UMo glass-ceramic in order to determine the nature of the crystalline phases. The examination was carried out using a Seifert 3000 diffractometer (GE Sensing, France) in the Bragg-Brentano geometry (2θ range: 10-95°; step 0.01°; time 15 s/step), equipped with a Cu source (λ = 0.15406 nm) (40 kV, 30 mA). The diffractograms were fitted by using the DIFFRAC^{plus} software and the PDF^{4+} database (Bruker, USA).

Scanning electron micrographs were collected on carbon-coated samples with a JEOL 6300 (JEOL, Japan) scanning electron microscope (SEM, 15 kV).

The Raman spectra were collected with a Horiba LabRAM HR800 micro-Raman spectrometer with a 532 nm excitation laser (green) located outside the hot cell and coupled with optical fibers to an optical microscope with an objective turret (from x1.25 to x100) (Optic Peter, France) implemented in the hot cell. The ×100 objective was used for non-polarized confocal Raman spectroscopy.

5 Results

5.1 Actinide content and homogeneity in the glass ceramics

The overall ^{241}Am and ^{244}Cm contents, obtained by isothermal calorimetry measurements are presented in Table 2 for the Am, Am/Nd and Cm-UMo glass ceramics. Concerning the Cm-UMo glass ceramic sample, this result was in very good agreement with the mean target doping value in ^{244}Cm. Concerning the glass ceramics containing ^{241}Am, the ^{241}Am content measured by calorimetry in the samples is slightly lower than the mean target doping value, by 3.8% for the Am-UMo sample and by 14.5% for the Am/Nd-UMo sample.

	measured by calorimetry (and compared to expected values)	
content in wt.%	^{241}Am	^{244}Cm
Am-UMo	1.59 (1.65)	
Am/Nd-UMo	0.71 (0.83)	
Cm-UMo		0.66 (0.65)

Table 2: ^{241}Am and ^{244}Cm content in the glass ceramics, determined by isothermal calorimetry and expressed in wt.%. Comparison with the mean targeted doping values, deduced from Table 1 and given between brackets.

Concerning the homogeneity of Am and Cm distributions measured by gamma spectrometry, with the exception of the bottom enrichment, the major part of the sample lengthwise (i.e. more than 50% of the length) has a homogeneous Am and Cm distribution, as illustrated in Figure 4 concerning the doped materials containing ^{241}Am and in Figure 5 concerning the ^{244}Cm-doped UMo matrix. This actinide enrichment of the bottom could be explained by the absence of mechanical stirring during the elaboration process that could favor a sedimentation of the heavy elements at high temperature. The relative enrichments observed in the bottom could thus explain the lower ^{241}Am content measured by calorimetry in the middle-part of the Am and Am/Nd-doped samples, compared to the mean target doping values. This difference in the ^{244}Cm amount was not observed in the case of the ^{244}Cm-UMo material because the enrichment area of the bottom was localized in a thinner part: 1 mm height compared (Figure 5) to around 3 mm height for the ^{241}Am-doped materials (Figure 4).

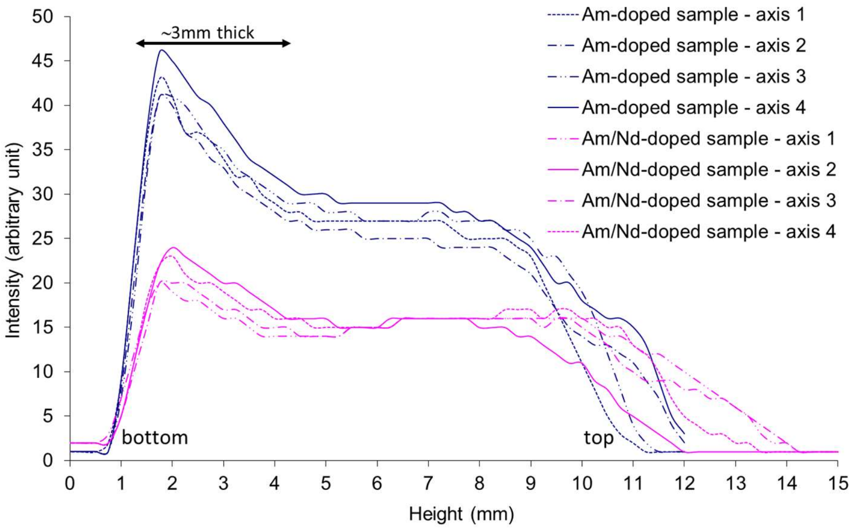

Figure 4: Evolution of the ^{241}Am gamma peak intensity versus the height of the sample according to 4 longitudinal axis .

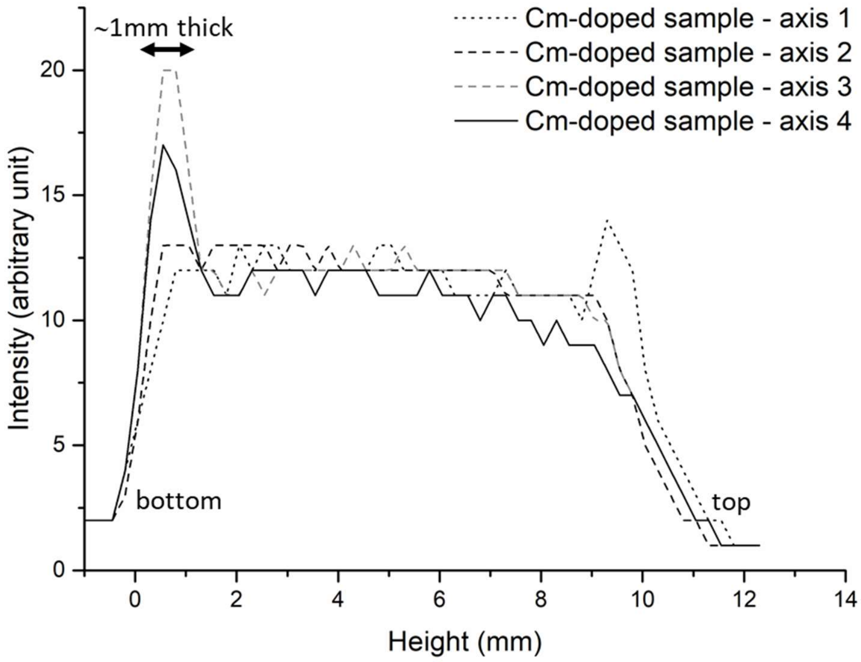

Figure 5: Evolution of the ^{244}Cm gamma peak intensity versus the height of the sample. Various longitudinal axis (expressed in degree) were explored.

To sum up, except the slight differences in the ^{241}Am content and the ^{241}Am and ^{244}Cm enrichments observed at the bottom of the rods (Figure 4 and Figure 5), the samples met expectations in terms of global Am and Cm mean incorporation in the samples. Moreover, as detailed in Table 2, the mean Am content in the Am/Nd-doped UMo glass-ceramic was qualitatively half the Am content measured in the Am-doped UMo glass-ceramic, as expected from Table 1.

5.2 Microstructure of the glass-ceramics after fabrication

The microstructure of the samples were characterized by both optical (Figure S1 in Supplementary Data) and electronic microscopies (Figure 6 and Figure 7). The different phases observed were identified by Raman spectroscopy (Figure 7 and Figure 8) and X-ray diffraction patterns (Figure 9). As similar microstructures were observed on all the samples, the following figures aim to illustrate the results without systematically presenting pictures for all of them.

Bubbles were present in the upper part of the samples (area A on Figure S1) and an important crystallization was noticed around the bubbles (not observable here, at this scale). At the vertical glass-ceramic / crucible interfaces, elongated dendritic shaped crystalline phases were observed (Figure 6-b and are B on Figure S1), which corresponds to the molybdate phase according to Raman spectroscopy (Figure 7). The microstructure of the center of each sample included small size phases of around 10-15 µm diameter (top part on Figure 6-b and Figure 7-d; area C on Figure S1). Finally, a sedimentation zone, containing rectangular base crystals ranging from ten to several hundred microns length, was observed at the bottom (Figure 6-a and Figure 7-a; area D on Figure S1): these crystalline phases are very similar to the one observed closed to the bubbles and are composed of the three crystalline phases molybdate, phosphate and zircon (Figure 7).

The SEM characterization with backscattered electrons shown the presence of heavy elements in all these secondary crystalline phases as they appeared in a lighter greyscale than the borosilicate residual glassy matrix (Figure 6 and Figure 7).

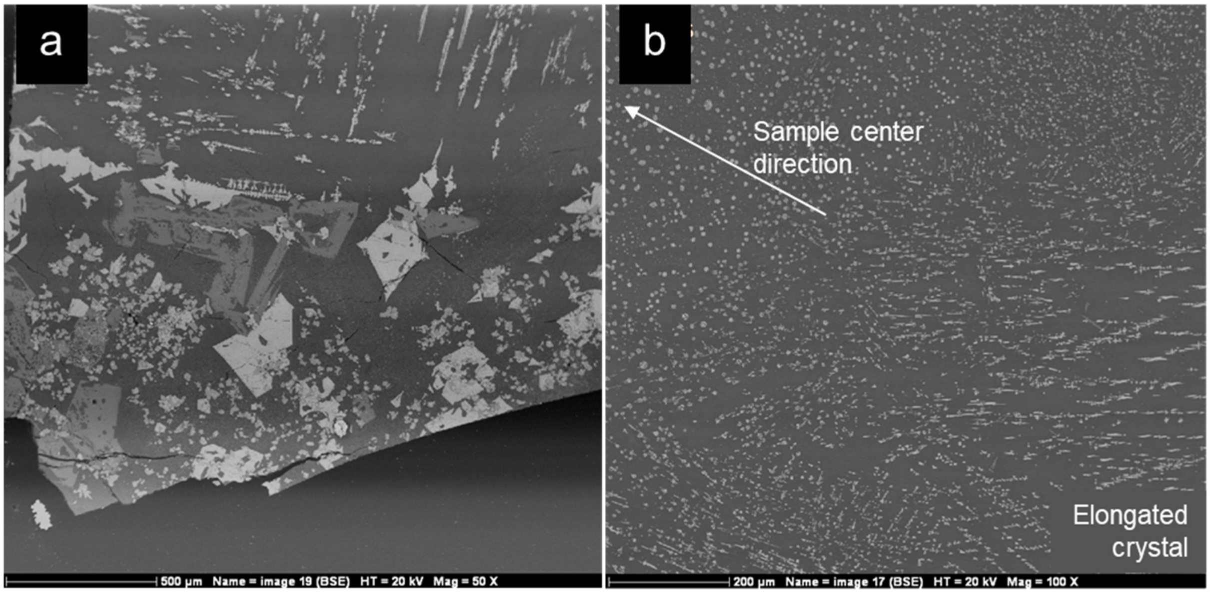

Figure 6: SEM micrographs (backscattered electrons) of the Am/Nd-doped UMo glass-ceramic sample: (a) the bottom part and (b) near the right side. White and light dark phases correspond to crystal phases and the dark grey corresponds to the embedding glassy phase.

The different phases were thus analyzed by Raman spectroscopy in confocal mode (Figure 7). Thus, this analysis allowed the determination of three kinds of Raman spectra corresponding to the following phases: calcium molybdate, zircon, calcium phosphate. A fourth Raman spectrum corresponding to the surrounding glassy phase (see Figure S2 in Supplementary Data) was obtained.

Raman spectra in agreement with molybdate [27] and phosphate phases [28-30] were observed everywhere in the samples, both in the clusters and in the zone of strong crystallization at the bottom of the glass ceramic samples. The phosphate phase presents two different spectra depending on the analyzed area (Figure 8). This can come from local changes in chemical composition and different crystal symmetries. This fact will be develop later, in the Discussion section. In addition, zircon and zirconia crystals (m-ZrO_2 for monoclinic zirconia, with the A_g peak at 476 cm^{-1}) were also identified [31-33] in the zone of strong crystallization at the bottom of the rod and sometimes in large crystallized clusters (Figure 7). The zirconia crystals were very small (<1 micron length) and were included in the zircon phase: in the Figure 7-d, they appear in a lighter greyscale in the zircon crystal.

Finally, the SEM characterization coupled with the Raman spectroscopy gave some valuable information on the crystalline phases observed on these samples. The use of Raman spectroscopy made it possible to go a step further in the description of the crystalline phases compared to the previous publication on this UMo material [13, 14, 16].

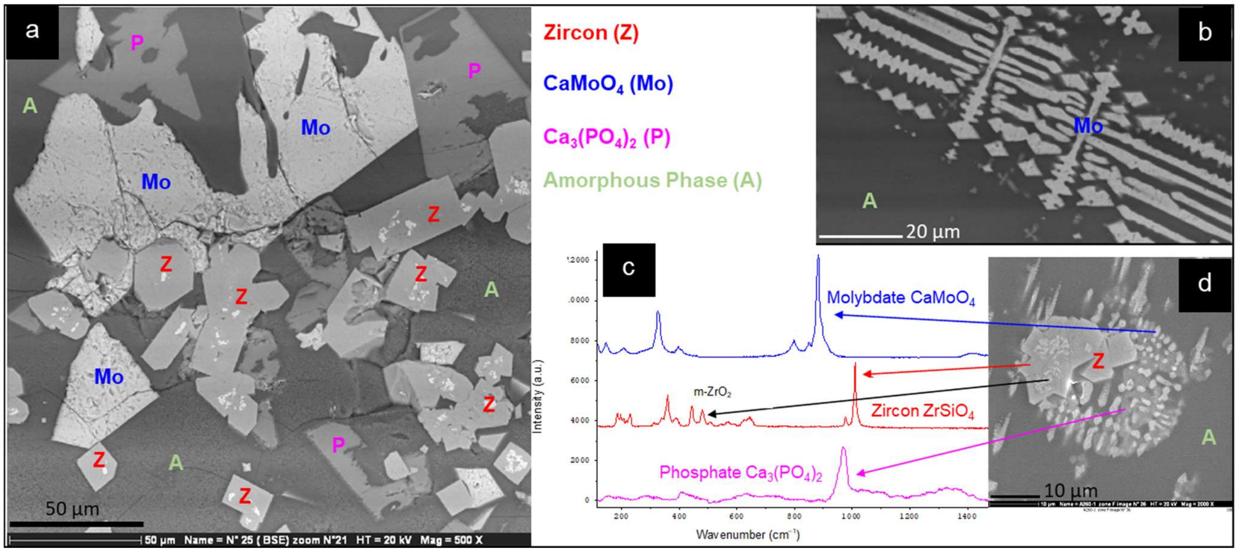

Figure 7: SEM micrographs (backscattered electrons) of the secondary phases and associated Raman spectra (zircon, calcium molybdate and calcium phosphate). (a) zoom (x 500) of the Figure 6-a) micrograph in the bottom part of the Am/Nd-doped UMo glass-ceramic, (b) zoom (x 1000) of the same sample in the right side, (c) and (d) are from the center of the Cm-doped UMo glass-ceramic (x 2000).

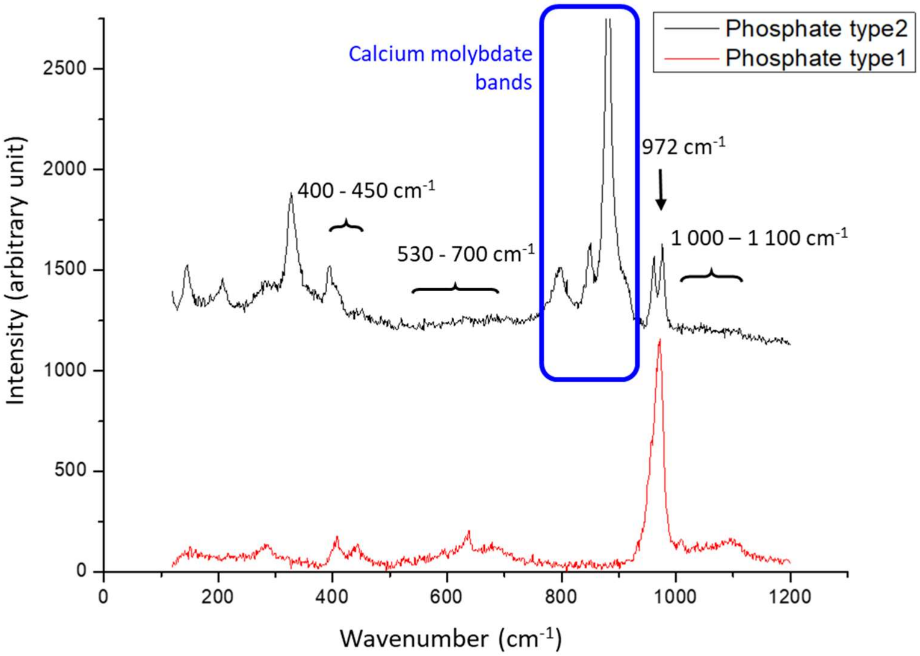

Figure 8: Example of the two types of Raman spectra found in the phosphate phase in the Cm-doped UMo glass-ceramic.

The X-ray diffraction patterns of the UMo samples, as illustrated for the Cm-doped UMo sample, (Figure 9), showed reflections assigned to calcium molybdate and zircon. The platinum crucible signal was also noticed on the Cm-doped sample as the crucible was not removed on this sample after fabrication (see Figure 3). No signal from the phosphate phase nor the m-ZrO_2 were observed.

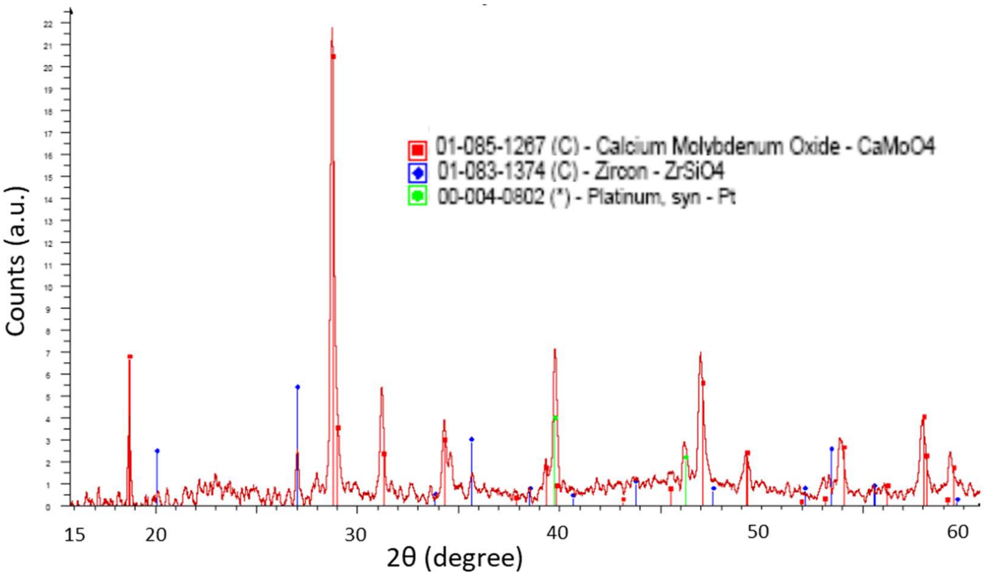

Figure 9: Cm-doped UMo glass-ceramic X-ray diffraction patterns. All the reflections were assigned using the PDF4+ database: in red, CaMoO$_4$; in green zircon crystal and in green platinum from the crucible (as described in Figure 3). No peaks were observed after 60°.

5.3 Am, Cm and Nd distribution in the glass-ceramics

The relative enrichments in Am, Cm and Nd in the crystallized phases and the embedding glass are presented qualitatively in the mapping pictures obtained on the Am/Nd-doped matrix (Figure 10) and from EPMA quantitative measurements (Table 3). A great enrichment in Am, Cm and Nd was observed in the phosphate and molybdate phases compared to the mean target doping value, the embedding borosilicate glass and the zircon phase (Table 4). No detectable amount of Am, Nd and Cm was even evidenced in the zircon phase.

In the molybdate phases, 1.2 at.% of Am was measured in the Am-UMo sample and a total of 0.99 at.% of (Am+Nd) was measured in the Am/Nd-UMo sample (Table 3). In the phosphate phases, 1.1 at.% of Am was measured in the Am-UMo sample and a total of 1.0 at.% of (Am+Nd) was measured in the Am/Nd-UMo sample. By taking into account the 10% uncertainty on the EPMA quantitative measurements of Am and Nd, it can be considered that these concentrations between the Am-UMo and the Am/Nd-UMo samples were similar, and therefore that similar enrichments were measured in both phosphate and molybdate phases concerning the Am and Am/Nd-doped UMo glass ceramics. Moreover, by analyzing the data in the Am/Nd-UMo sample, Am and Nd remained globally equally distributed in these different phases (0.54/0.45 of Am/Nd in at.% in the molybdate phases and 0.47/0.53 in the phosphate phases), compared to the theoretical relative doping (half Am/half Nd).

Concerning the Cm-UMo glass ceramic (Table 3), in both the molybdate and the phosphate phases, Nd was in slightly lower quantity versus Cm (Cm/Nd ~ 3.5 in the molybdate phase and Cm/Nd ~ 4.3 in the phosphate phase) than expected from the mean target doping value (Cm/Nd=3, Table 3). Furthermore, the phosphate phase seemed slightly enriched in both Cm and Nd compared to the molybdate phase. All these observations could be due to less statistics in the measurements as only 10 quantitative measurements were performed on each phase of this Cm-doped UMo sample, compared to around 50 quantitative measurements on each phase of the Am-doped samples. Indeed, in the molybdate phase, by taking into account the 10% uncertainty on the EPMA quantitative measurements, the measured Cm/Nd values, ranging from 2.9 to 4.3 could overlay the mean target doping value of 3.0.

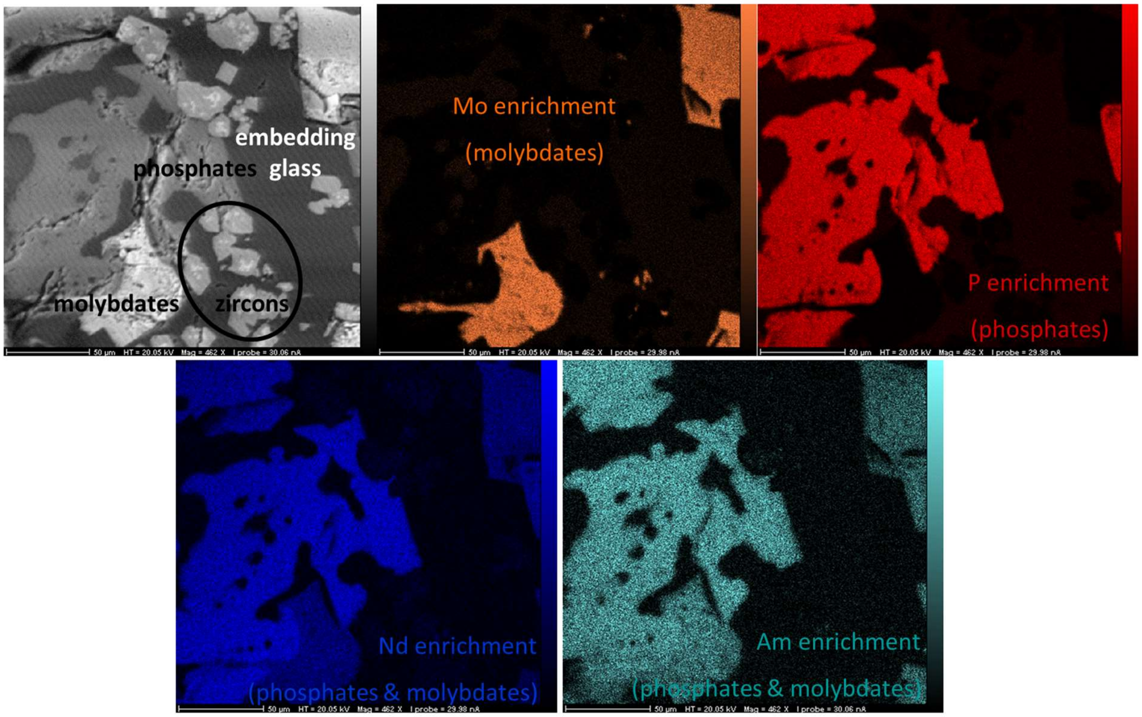

Figure 10: Electronic microprobe mapping of the Am/Nd-doped UMo.

at %		Am-UMo	Am/Nd-UMo	Cm-UMo
mean target doping value	Am	0.152	0.076	
	Nd		0.076	0.025
	Cm			0.075
molybdate	Am	1.2	0.54	
	Nd		0.45	0.15
	Cm			0.65
phosphate	Am	1.1	0.47	
	Nd		0.53	0.25
	Cm			0.88
zircon	Am	< LOD	*	
	Nd		*	*
	Cm			*
embedding glass	Am	0.05 ± 0.03	*	
	Nd		*	0.01 ± 0.01
	Cm			0.06 ± 0.02

*Table 3: EPMA quantitative data concerning Am, Nd and Cm atomic concentrations in the different phases of the UMo glass-ceramics. * = not measured. Uncertainties were of 10% when they are not specified.*

6 Discussion

This discussion aims to focus first on the UMo-samples microstructure and second on the (Am, Cm)/Nd incorporation and partitioning.

Regarding the phosphate phase microstructure, two types of Raman spectra were observed as described in Figure 8. These two kinds of Raman spectra showed some similar bands with a main one located around 972 cm^{-1} and other contributions around 400-450, 530-600 and 1000-1100 cm^{-1}. The main peak situated around 972 cm^{-1} corresponds to an orthophosphate compound, with isolated PO_4^{3-} [28]. Moreover, these bands are in agreement with the internal vibration modes of the free PO_4^{3-} [29], observed as follows: ν_1 = 938 cm^{-1}, ν_2 = 420 cm^{-1}, ν_3 = 1017 cm^{-1} and ν_4 = 567 cm^{-1}. The ν_1 and ν_3 modes correspond to elongations of the P–O bonds and the ν_2 and ν_4 modes correspond to angular deformation (O–P–O) [30]. All these modes are Raman active. The signatures of these two kinds of Raman spectra could thus correspond either to a monazite-type phase, containing actinides and/or Nd [34, 35], either to a calcium phosphate phase [28, 29, 36-38]. Concerning the type-2 Raman spectrum (in black on Figure 8), a double peak was observed around 950 cm^{-1}. This could correspond to a possible Ca substitution by Na [39, 40] or to an allotropic calcium phosphate (β phase instead of α) [41]. Note that the $NaCaPO_4$ phase studied by Gbureck et al. has a stoichiometry compatible with the present EPMA results in the UMo matrix, with almost identical contents of Na, Ca, P in the phosphate phase (results presented in the Table T2 in Supplementary Data). The EPMA failed to detect Mg, which rules out the hypothesis of a Merrillite-like phase. In conclusion, it remained difficult to conclude on the exact nature of the type-2 phosphatic phase observed in the UMo matrix: a weak substitution of Ca by Na, a solid solution in the Rhenanite structure with less sodium than calcium or a β -type calcium phosphate are all possible.

Regarding (Am,Cm)/Nd incorporation in the sample and their partitioning in the different phases (i.e. the crystalline phases and the embedding glassy matrix), the isothermal calorimetry results gave a global view of the samples whereas the EPMA measurements allows to focus on their partitioning in the different phases at the micron scale. As the global Am and Cm incorporation in the samples met expectations, the EPMA results can be compared to the mean target doping value given in Table 1. A partition coefficient can be calculated by applying Equation 1 and is presented in Table 4. Two main results can be highlighted from these EPMA measurements.

Firstly, it is obvious that Nd can be considered as a relevant surrogate of both Am and Cm as the Nd/actinide mean target doping values is relatively well preserved in the molybdate and the phosphate phases. This similar behavior was also observed on another glass-ceramic wasteform having silicate apatite crystals, in which comparison on Nd and Am incorporation was recently studied [4]. Therefore, further studies can thus be performed on such non-radioactive UMo materials, by using Nd instead of trivalent actinides.

Secondly, a preferential incorporation of Nd, Am and Cm was clearly observed in the phosphate and the molybdate phases, with a partition coefficient ranging from 6 to 12 (Table 4). The great ability of crystalline phases to incorporate actinides is known in the literature [3, 42]. In these crystalline materials, actinides occupy specific atomic positions in the periodic structure. This allows high loadings of these actinides, but it imposes suitable ionic radius, charge, and bonding constraints in order them to be successfully incorporated in the crystalline structures. Some authors showed the ability of $CaMoO_4$ to incorporate neodymium or others trivalent rare earth elements [15, 43, 44]. They assumed

[15, 43] or observed [44] that this result could be extended to trivalent actinides. Concerning the phosphate phase, monazite-like structures can incorporated high amount of trivalent actinides [45]. Finally, the greater ability for trivalent actinides or Nd to be incorporated in the crystalline structure instead of the embedding glass matrix was already observed in quite similar glass ceramics [4]. It is thus not surprising here to observe their favored incorporation in these molybdate and phosphate phases compared to the embedded glass matrix.

Glass-ceramic	Am -UMo	Am/Nd-UMo		Cm-UMo	
Considered doping element	Am	Am	Nd	Cm	Nd
Molydbate phase	x (7.9 ± 0.8)	x (7.1 ± 0.7)	x (5.9 ± 0.6)	x (8.7 ± 0.9)	x (6.0 ± 0.6)
Phosphate phase	x (7.3 ± 0.8)	x (6.2 ± 0.6)	x (7.0 ± 0.7)	x (11.8 ± 1.2)	x (10.0 ± 1.0)

Table 4 : Partition coefficients of Am, Cm and Nd in the phosphate and the molybdate phases of the studied glass ceramics, calculated from Equation 1.

Finally, this preferential partitioning of trivalent actinides in phosphate and molybdate phases compared to the embedded glass matrix is a crucial result with regard to the ageing of the UMo-matrix. Indeed, the damage caused by alpha-decay would entirely take place in these two crystalline phases. Thanks to this work, the level of nuclear dose induced by Am alpha-decay in these crystalline phases can be calculated versus time and versus the amount of Am incorporated in the UMo matrix, by using the partition coefficient around x 6 – 7 for Am in these two crystalline phases previously measured (Table 4).

7 Conclusion

In this paper, we considered four glass-ceramics fabricated in hot cell and containing Nd and/or trivalent actinides (Am; Cm). This type of glass-ceramic is composed of crystalline phases, which are phosphates, molybdates and zircons, embedded in a durable borosilicate matrix. The overall ^{241}Am and ^{244}Cm contents in the samples, measured by isothermal calorimetry, were consistent with the expected global doping rates. Concerning the ^{241}Am and ^{244}Cm longitudinal distribution in the cylindrical rods, except a slight enrichment in the bottoms correlated to a high amount of crystalline phases, the major part of the sample lengthwise showed a homogeneous Am and Cm distribution. However, the microstructure of the sample was heterogeneous as expected, with the presence of phosphate, molybdate and zircon phases embedded in a glassy matrix. Nd behaved like trivalent actinides in these UMo matrices and can thus be considered as a relevant surrogate of trivalent actinides in terms of incorporation, location and resulting microstructure in the UMo matrix. In conclusion, the strategy consisting in using Nd as a surrogate for studies carried out in non-radioactive environments, including at a full industrial scale [14], is validated by the results presented in the present work.

Finally, a higher Am, Cm and Nd partitioning was observed in the phosphate and molybdate phases compared to the embedding borosilicate glass and the zircon phase. This is identified by a partition coefficient around x 6 – 7 for Am and Nd in these two crystalline phases compared to the mean target doping value. To go further, as Am has preferential locations in the UMo matrix, the alpha decay dose received by these phases could be potentially high enough to suspect changes in their structure and macroscopic properties [46-48]. Ageing studies by considering the ^{244}Cm-doped UMo matrix would be of first importance to assess the consequences of such doses on the integrity of the UMo matrix – mostly on the crystalline phases and their vicinity – versus time.

8 Acknowledgments

The authors would like to thank Orano for its financial support and all the LMPA team for their work performed in the hot cells of DHA unit of ATALANTE facility. They also would like to thank D. Roudil and R. Caraballo, now retired, for their contribution on sample preparation and Raman characterization.

9 References

1. IAEA, *Status and Trends in Spent Fuel and Radioactive Waste Management*, ed. N.E.S.N. NW-T-1.14. 2018, Vienna.
2. Gin, S., et al., *Radionuclides containment in nuclear glasses: an overview.* Radiochimica Acta, 2017. **105**(11): p. 927-959.
3. Weber, W.J., et al., *Materials Science of High-Level Nuclear Waste Immobilization.* Mrs Bulletin, 2009. **34**(1): p. 46-53.
4. Bardez-Giboire, I., et al., *Americium and trivalent Lanthanides incorporation in high-level waste glass-ceramics.* Journal of Nuclear Materials, 2017. **492**: p. 231-238.
5. Caurant, D. and O. Majérus, *Glasses and Glass-Ceramics for Nuclear Waste Immobilization*, in *Encyclopedia of Materials: Technical Ceramics and Glasses*, M. Pomeroy, Editor. 2021, Elsevier: Oxford. p. 762-789.
6. Donald, I.W., B.L. Metcalfe, and R.N.J. Taylor, *The immobilization of high level radioactive wastes using ceramics and glasses.* Journal of Materials Science, 1997. **32**(22): p. 5851-5887.
7. Delaye, J.M., et al., *Molecular dynamics simulation of radiation damage in glasses.* Journal of Non-Crystalline Solids, 2011. **357**(14): p. 2763-2768.
8. Miro, S., et al., *Monitoring of alpha-decay radiation damage in a 241Am-doped glass-ceramic material.* Journal of Nuclear Materials, 2023. **580**: p. 154397.
9. Jantzen, C.M. and M.I. Ojovan, *On Selection of Matrix (Wasteform) Material for Higher Activity Nuclear Waste Immobilization (Review).* Russian Journal of Inorganic Chemistry, 2019. **64**(13): p. 1611-1624.
10. Ojovan, M.I., V.A. Petrov, and S.V. Yudintsev *Glass Crystalline Materials as Advanced Nuclear Wasteforms*. Sustainability, 2021. **13**, DOI: 10.3390/su13084117.
11. Caurant, D., et al., *Effect of molybdenum on the structure and on the crystallization of SiO2-Na2O-CaO-B2O3 glasses.* JOURNAL OF THE AMERICAN CERAMIC SOCIETY, 2007. **90**(3): p. 774-783.
12. Magnin, M., et al., *Effecto of compositional changes on the structure and crystallization tendency of a borsilicate glass containing* MoO_3, in *Environmental Issues And Waste Management Technologies In The Materials And Nuclear Industries XII*. 2009.
13. Pinet, O., et al., *Glass matrices for immobilizing nuclear waste containing molybdenum and phosphorus.* JOURNAL OF NUCLEAR MATERIALS, 2008. **377**(2): p. 307-312.
14. Pinet, O., et al., *Glass ceramic for the vitrification of high level waste with a high molybdenum content.* JOURNAL OF NUCLEAR MATERIALS, 2019. **519**: p. 121-127.
15. Henry, N., et al., *Heat treatments versus microstructure in a molybdenum-rich borosilicate.* Journal of Non-Crystalline Solids, 2004. **333**(2): p. 199-205.
16. Schuller, S., et al., *Phase separation and crystallization of borosilicate glass enriched in MoO3, P2O5, ZrO2, CaO.* Journal of Non-Crystalline Solids, 2008. **354**(2): p. 296-300.
17. Vance, E.R., et al., *Leaching behaviour of and Cs disposition in a UMo powellite glass–ceramic.* Journal of Nuclear Materials, 2014. **448**(1): p. 325-329.

18. Kidari, A., et al., *Solubility and partitioning of minor-actinides and lanthanides in alumino-borosilicate nuclear glass.* Atalante 2012 International Conference on Nuclear Chemistry for Sustainable Fuel Cycles, 2012. **7**: p. 554-558.
19. Peuget, S., et al., *Effect of alpha radiation on the leaching behaviour of nuclear glass.* Journal of Nuclear Materials, 2007. **362**(2-3): p. 474-479.
20. Peuget, S., J.M. Delaye, and C. Jegou, *Specific outcomes of the research on the radiation stability of the French nuclear glass towards alpha decay accumulation.* Journal of Nuclear Materials, 2014. **444**(1-3): p. 76-91.
21. De Echave, T., et al., *Effect of clayey groundwater on the dissolution rate of SON68 simulated nuclear waste glass at 70 degrees C.* Journal of Nuclear Materials, 2018. **503**: p. 279-289.
22. Tribet, M., et al., *Leaching of a zirconolite ceramic waste-form under proton and He2+ irradiation.* Radiochimica Acta, 2008. **96**(9-11): p. 619-624.
23. Mitamura, H., et al., *ALPHA-DECAY DAMAGE EFFECTS IN CURIUM-DOPED TITANATE CERAMIC CONTAINING SODIUM-FREE HIGH-LEVEL NUCLEAR WASTE.* JOURNAL OF THE AMERICAN CERAMIC SOCIETY, 1994. **77**(9): p. 2255-2264.
24. Wiss, T., et al., *Helium release from plutonium and curium-doped zirconolite.* Journal of Nuclear Materials, 2007. **362**(2): p. 431-437.
25. Peuget, S., et al., *Irradiation stability of R7T7-type borosilicate glass.* Journal of Nuclear Materials, 2006. **354**(1-3): p. 1-13.
26. Fillet, S., et al., *Leaching of Actinides from the French LWR Reference Glass.* Material Research Society Symposium Proceedings, 1985. **50**: p. 211–218.
27. Brinkman, K., et al., *Single phase melt processed powellite (Ba,Ca)MoO4 for the immobilization of Mo-rich nuclear waste.* Journal of Alloys and Compounds, 2013. **551**: p. 136-142.
28. Popović, L., D. de Waal, and J.C.A. Boeyens, *Correlation between Raman wavenumbers and P⍰O bond lengths in crystalline inorganic phosphates.* Journal of Raman Spectroscopy, 2005. **36**(1): p. 2-11.
29. de Aza, P.N., et al., *Vibrational Properties of Calcium Phosphate Compounds. 1. Raman Spectrum of β-Tricalcium Phosphate.* Chemistry of Materials, 1997. **9**(4): p. 912-915.
30. Dekhili, R., et al., *Raman spectra in LiH2PO4 and KLi(H2PO4)2: Mode assignment.* Journal of Raman Spectroscopy, 2019. **50**(3): p. 447-453.
31. Ji, P., et al., *Direct Observation of Enhanced Raman Scattering on Nano-Sized ZrO2 Substrate: Charge-Transfer Contribution.* Frontiers in Chemistry, 2019. **7**.
32. Atkinson, I., O.C. Mocioiu, and E.M. Anghel, *A study of zircon crystallization, structure, and chemical resistance relationships in ZrO_2 containing ceramic glazes.* Boletín de la Sociedad Española de Cerámica y Vidrio, 2022. **61**(6).
33. Kim, B.K. and H.O. Hamaguchi, *Mode assignments of the Raman spectrum of monoclinic zirconia by isotopic exchange technique.* PHYSICA STATUS SOLIDI B-BASIC RESEARCH, 1997. **203**(2): p. 557-563.
34. Bregiroux, D., et al., *Solid-State Synthesis of Monazite-type Compounds Containing Tetravalent Elements.* Inorganic Chemistry, 2007. **46**(24): p. 10372-10382.
35. Silva, E.N., et al., *Vibrational Spectra of Monazite-Type Rare-Earth Orthophosphates.* Optical Materials, 2006. **29**: p. 224-230.
36. Xie, X., et al., *Natural high-pressure polymorph of merrillite in the shock veins of the Suizhou meteorite.* Geochimica et Cosmochimica Acta, 2002. **66**(13): p. 2439-2444.
37. Zhai, S., et al., *Synthesis and characterization of strontium–calcium phosphate γ-Ca3−xSrx(PO4)2 (0≤x≤2).* Materials Chemistry and Physics, 2010. **120**(2): p. 348-350.
38. Fix, W., H. Heymann, and R. Heinke, *Subsolidus Relations in the System 2CaO·SiO2-3CaO·P2O5.* Journal of the American Ceramic Society, 1969. **52**(6): p. 346-347.
39. Gbureck, U., et al., *Antimicrobial potency of alkali ion substituted calcium phosphate cements.* Biomaterials, 2005. **26**(34): p. 6880-6886.

40. Quillard, S., et al., *Structural and spectroscopic characterization of a series of potassium-and/or sodium-substituted β-tricalcium phosphate.* Acta Biomaterialia, 2011. **7**(4): p. 1844-1852.
41. Jillavenkatesa, A. and R.A. Condrate, *The Infrared and Raman Spectra of β-and α-Tricalcium Phosphate (Ca3(Po4)2).* Spectroscopy Letters, 1998. **31**(8): p. 1619-1634.
42. Ewing, R.C. and W. Lutze, *High-level nuclear waste immobilization with ceramics.* Ceramics International, 1991. **17**(5): p. 287-293.
43. Patil, D.S., et al., *Impact of rare earth ion size on the phase evolution of MoO3-containing aluminoborosilicate glass-ceramics.* Journal of Nuclear Materials, 2018. **510**: p. 539-550.
44. Bosbach, D., et al., *Trivalent actinide coprecipitation with powellite (CaMoO4): Secondary solid solution formation during HLW borosilicate-glass dissolution.* Radiochimica Acta, 2004. **92**(9-11): p. 639-643.
45. Holliday, K.S., et al., *Site-selective time resolved laser fluorescence spectroscopy of Eu and Cm doped LaPO4.* 2012. **100**(3): p. 189-195.
46. Meldrum, A., et al., *Radiation damage in zircon and monazite.* Geochimica et Cosmochimica Acta, 1998. **62**(14): p. 2509-2520.
47. Wang, X., et al., *Irradiated rare-earth-doped powellite single crystal probed by confocal Raman mapping and transmission electron microscopy.* JOURNAL OF RAMAN SPECTROSCOPY, 2014. **45**(5): p. 383-391.
48. Patel, K.B., et al., *Discovery of a maximum damage structure for Xe-irradiated borosilicate glass ceramics containing powellite.* JOURNAL OF NUCLEAR MATERIALS, 2018. **510**: p. 229-242.